A three-dimensional surface wave–ocean circulation coupled model and its initial testing

**Fangli Qiao · Yeli Yuan · Tal Ezer · Changshui Xia ·
Yongzeng Yang · Xingang Lü · Zhenya Song**

Abstract A theoretical framework to include the influences of nonbreaking surface waves in ocean general circulation models is established based on Reynolds stresses and fluxes terms derived from surface wave-induced fluctuation. An expression for the wave-induced viscosity and diffusivity as a function of the wave number spectrum is derived for infinite and finite water depths; this derivation allows the coupling of ocean circulation models with a wave number spectrum numerical model. In the case of monochromatic surface wave, the wave-induced viscosity and diffusivity are functions of the Stokes drift. The influence of the wave-induced mixing scheme on global ocean circulation models was tested with the Princeton Ocean Model, indicating significant improvement in upper ocean thermal structure and mixed layer depth compared with mixing obtained by the Mellor–Yamada scheme without the wave influence. For example, the model–observation correlation coefficient of the upper 100-m temperature along 35° N increases from 0.68 without wave influence to 0.93 with wave influence. The wave-induced Reynolds stress can reach up to about 5% of the wind stress in high latitudes, and drive 2–3 Sv transport in the global ocean in the form of mesoscale eddies with diameter of 500–1,000 km. The surface wave-induced mixing is more pronounced in middle and high latitudes during the summer in the Northern Hemisphere and in middle latitudes in the Southern Hemisphere.

Keywords Surface wave · Wave-induced mixing ·
Ocean circulation · Mixed layer

F. Qiao (✉) · Y. Yuan · C. Xia · Y. Yang · X. Lü · Z. Song
Key Laboratory of Marine Science and Numerical Modeling
(MASNUM), First Institute of Oceanography,
State Oceanic Administration,
Qingdao, China
e-mail: qiaofl@fio.org.cn

T. Ezer
Old Dominion University,
Norfolk, VA 23529, USA

1 Introduction

An accurate representation of the upper ocean mixing processes and thus the oceanic surface mixed layer (ML) is important for ocean circulation models, whether they are aimed at small-scale coastal simulations or for large-scale global climate simulations. The vertical mixing in many three-dimensional numerical ocean circulation models are often based on turbulence closure schemes, such as the widely used Mellor–Yamada (M-Y) scheme (Mellor and Yamada 1982). However, a common problem of such schemes is an underestimation of the vertical mixing in upper layer and the mixed layer depth. Thus, the sea surface temperature (SST) is often overestimated, ML is too shallow, and the strength of seasonal thermocline is underestimated, especially during summer (Martin 1985; Kantha and Clayson 1994; Ezer 2000; Mellor 2001). The oceans contain nearly all of the thermal content of the coupled ocean–atmosphere system and are regarded as the flywheel of climate fluctuations. ML is particularly important to the process of atmosphere–ocean interaction, e.g., in El Niño–Southern Oscillation prediction models. Therefore, better parameterization of diapycnal mixing in the upper oceans in climate models is important in improving our understanding of the atmosphere–ocean system.

Initial attempts to improve mixing under very stable stratification conditions assumed that processes such as

internal waves at the bottom of the ML are not well represented in the M-Y scheme (or most other mixing schemes used in ocean models). Adding either a Richardson number-dependent mixing below the ML (Kantha and Clayson 1994) or a Richardson number-dependent dissipation (Ezer 2000; Mellor 2001) show some positive results, in particular when also using high-frequency winds and adding short-wave radiation penetration under the surface (Ezer 2000). However, the effects of those changes are limited and there is evidence from different models that there is still insufficient mixing in the upper ocean for ocean models.

Recently, a new focus has been put on the contribution of surface waves to oceanic mixing and on wave–current–turbulence interaction processes (Craig and Banner 1994; Terray et al. 1996; Stacey 1999; Burchard 2001; Malcherek 2003; Mellor 2003, 2008; Mellor and Blumberg 2004; Kantha and Clayson 2004; Ardhuin and Jenkins 2006). Including the mixing effects associated with the breaking of surface waves can be applied to ocean models by using surface boundary conditions (Craig and Banner 1994; Terray et al. 1996; Stacey 1999; Mellor and Blumberg 2004; Kantha and Clayson 2004). Although those studies indicate some improvement in simulated ML, SST and surface currents, the breaking wave effects are mostly limited to the top few meters near the surface and may require very fine vertical resolution in the surface layers of the model. A more complicated problem is how to represent the vertical distribution of the wave–circulation interaction in three-dimensional ocean circulation models. A step in this direction has been recently taken by Mellor (2003, 2008) who developed a set of wave–circulation interaction equations. Mellor's scheme introduces the production of turbulence by wave–current interaction, while the original M-Y scheme only includes shear and buoyancy turbulence production. This new scheme, as well as other approaches now under development, has not yet been fully implemented or tested in ocean models.

Here, a simpler mixing parameterization approach is proposed, by deriving Reynolds stress expressions introducing a wave mixing coefficient which is added to the shear-induced turbulence mixing coefficient of the M-Y scheme (or any other scheme such as K-Profile Parameterization, KPP hereafter). Phillips (1961) pointed out that "although the use of potential theory has been very successful in describing certain aspects of the dynamics of gravity waves, it is known that in a real fluid the motion cannot be truly irrotational." Wave-induced motion has the potential to increase mixing beyond the classical production of turbulence by the mean current shear. While the exact mechanism of wave–turbulence interaction is not fully understood, the underlying assumption here is that some wave-induced motions may have scales comparable to that

of shear-induced turbulence, thus we use the correlation between wave-induced motion and shear-induced turbulence to drive a parameterization and designate it as the wave-induced mixing coefficient. Although the horizontal scales of surface gravity waves, with the order of ~100 m, is much smaller than the scales of horizontal ocean circulation, the scale of the wave-induced vertical velocity in the upper ocean can be comparable or even greater than vertical velocity variations. A recent derivation of wave–energy equations by Malcherek (2003) also introduces similar wave eddy viscosity concept. For monochromatic surface wave, the wave-induced vertical mixing decays with the depth away from the surface in the form of e^{3kz} (with k as the wave number) which is exactly the same as that deduced from Anis and Moum's observation (Anis and Moum 1995; Huang and Qiao 2010). Our wave-induced viscosity (or diffusivity) is the function of the wave number spectrum which can be easily obtained from a third-generation wave number spectrum numerical model (Yuan et al. 1991; Donelan and Yuan 1994; Yang et al. 2005). This approach allows the coupling of a wave model with an ocean circulation model. While many different approaches for the wave–turbulence interaction parameterizations are being developed, preliminary testing of our approach shows that the additional wave-induced mixing significantly improves the model ML and SST, when compared with model runs without the wave effects.

A wave-induced mixing penetration depth D_5 is defined as the depth at which the surface wave-induced viscosity decreases to 5 cm^2 s^{-1}. The wave number spectral model results indicate that D_5 can reach to nearly 100 m in high latitude and about 30 m in tropical areas (Qiao et al. 2004a). In fact, a large part of the global deep ocean has vertical mixing in the order of 0.1 cm^2 s^{-1}. The wave–circulation coupled model has shown satisfactory performances in a series of circulation modeling studies in the Yellow Sea and East China Sea (Qiao et al. 2004b, 2006; Lü et al. 2006; Xia et al. 2006). Preliminary results even indicate that the wave-induced mixing can improve a common problem in climate models known as the "too cold tongue" in the tropical Pacific (Song et al. 2007). Based on similar ideas to those proposed here and on observation, Babanin (2006) suggested that wave motion may generate additional turbulence beyond that associated with breaking waves and showed the existence of nonbreaking wave-induced turbulence from skillful measurements (Babanin and Haus 2009), and their experimental approximation is also consistent with the $e \sim a^3$ dependence implied by Qiao et al. (2004a, 2008). Observation in the East China Sea (Matsuno et al. 2006) indicates that the vertical profiles of diffusivity are in accord with the theoretical results of Qiao et al. (2004a). Application in Bohai Sea of the wave-induced vertical mixing showed much improved tempera-

ture simulations (Lin et al. 2006). However, the note of wave-induced vertical mixing by Qiao et al. (2004a) is a too simplified version of the parameterization suggested here: the previous formulation of wave-induced mixing coefficient, B_V, did not include shallow-water regime; little discussion was made on the wave-induced Reynolds stress which also transfers energy from wave to currents; only limited numerical applications were given due to paper length limitation.

In this paper, we describe the method of parameterization for the wave–circulation coupled model in Section 2. The method is then applied into a global implementation of the Princeton Ocean Model (POM) in Section 3 (implementation in several other models has been completed with similar results, but for lack of space will not be reported here). Discussion and conclusions conclude the paper.

2 Basic theory

Ocean surface waves play an important role in the processes of heat, momentum, and material fluxes between the double systems of atmosphere and ocean. Surface waves influence ocean circulation system mainly through two ways: (1) Both wave breaking and wave-induced vertical movement stir the upper ocean and, as a consequence, enhance the viscosity and diffusivity coefficients of the ocean circulation processes. Most of the previous studies focus on the wave-breaking process, while the present work discusses the mixing induced by the vertical wave motion (hereinafter, the wave-induced mixing). (2) Three-dimensional wave-induced Reynolds stress transfers kinematic energy from surface waves to ocean circulation.

2.1 Governing equations of ocean circulation

For the study of wave–circulation coupling, the ocean circulation elements including velocity, temperature, and salinity are commonly separated into a mean (upper case) and a fluctuation (lower case). The governing equations of ocean circulation at the mean state can be written as:

$$
\begin{aligned}
&\frac{\partial U_i}{\partial x_i} = 0 \\
&\frac{\partial U_j}{\partial t} + U_k \frac{\partial U_j}{\partial x_k} + \varepsilon_{jkl} f_k U_l = \frac{\partial}{\partial x_k}\left(-\langle u_k u_j \rangle\right) + \frac{\partial}{\partial x_k}\left(\nu E_{ik}\right) - \frac{1}{\rho_0}\frac{\partial P}{\partial x_j} - g_j \frac{\rho}{\rho_0} \\
&\frac{\partial T}{\partial t} + U_k \frac{\partial T}{\partial x_k} = \frac{\partial}{\partial x_k}\left(-\langle u_k \theta \rangle\right) + \frac{\partial}{\partial x_k}\left(\kappa \frac{\partial T}{\partial x_k}\right) \\
&\frac{\partial S}{\partial t} + U_k \frac{\partial S}{\partial x_k} = \frac{\partial}{\partial x_k}\left(-\langle u_k s \rangle\right) + \frac{\partial}{\partial x_k}\left(D \frac{\partial S}{\partial x_k}\right) \\
&\rho = \rho(T, S, P)
\end{aligned}
\tag{1}
$$

where x_1, x_2, and x_3 indicate the x, y, and z axes of the Cartesian coordinates, respectively, U_i and P are the mean

current components and pressure, respectively, u_i is the fluctuation velocity, T and S represent the mean temperature and salinity, respectively, θ and s are their fluctuations, respectively, f and g are the Coriolis parameter and gravitational acceleration, respectively, ν, κ, and D are the molecular viscosity coefficient, molecular heat diffusivity, and molecular salt diffusivity, respectively, and $E_{il} = \frac{\partial U_i}{\partial x_l} + \frac{\partial U_l}{\partial x_i}$.

We separate the velocity fluctuation into a current-related part (c) and a wave-induced part (w) (Yuan et al. 1999), i.e.:

$$
u_i = u_{iw} + u_{ic}.
\tag{2}
$$

Then, the Reynolds stress can be expressed as:

$$
-\langle u_i u_j \rangle = -\langle u_{iw} u_{jw} \rangle - \langle u_{iw} u_{jc} \rangle - \langle u_{ic} u_{jw} \rangle - \langle u_{ic} u_{jc} \rangle
\tag{3}
$$

and the Reynolds fluxes of temperature and salinity are:

$$
-\langle u_i \theta \rangle = -\langle u_{iw} \theta \rangle - \langle u_{ic} \theta \rangle,
\tag{4}
$$

$$
-\langle u_i s \rangle = -\langle u_{iw} s \rangle - \langle u_{ic} s \rangle.
\tag{5}
$$

In Eq. 3, $-\langle u_{iw} u_{jw} \rangle$ is the wave-induced Reynolds stress, $-[\langle u_{iw} u_{jc} \rangle + \langle u_{ic} u_{jw} \rangle]$ is the momentum mixing induced by surface wave motion, and $-\langle u_{ic} u_{jc} \rangle$ is the turbulence Reynolds stress generally considered in ocean circulation models. In Eqs. 4 and 5, $-\langle u_{iw} \theta \rangle$ and $-\langle u_{iw} s \rangle$ are the wave-induced Reynolds fluxes for temperature and salinity, respectively, while $-\langle u_{ic} \theta \rangle$ and $-\langle u_{ic} s \rangle$ represent the Reynolds fluxes for temperature and salinity, respectively.

In order to deal with the wave-related parts of Eqs. 3, 4, and 5, the expression of ocean surface wave velocity is described in the following section.

2.2 The linear ocean wave theory in the deep/infinite ocean

The main features of ocean surface waves in the deep ocean can be described by the following linear equations:

$$
\begin{array}{lll}
\Delta \phi = 0 & z \leq 0 & \text{(a)}, \\
\{u_{1w}, u_{2w}, u_{3w}\} = \nabla \phi & z \leq 0 & \text{(b)}, \\
\frac{\partial \zeta}{\partial t} = \frac{\partial \phi}{\partial z} & z = 0 & \text{(c)}, \\
\frac{\partial \phi}{\partial t} + g\zeta = 0 & z = 0 & \text{(d)}, \\
|\nabla \phi| = 0 & z \to -\infty & \text{(e)}
\end{array}
\tag{6}
$$

where ϕ is the velocity potential function, u_{1w}, u_{2w}, and u_{3w} are the wave velocity components at the x, y, and z directions, respectively, and ζ is the surface wave elevation. For the surface wave, z is upward positive and $z=0$ at the mean sea level.

Assuming that the ocean wave is a stationary and locally uniform process, then the surface elevation of the ocean wave can be expressed in terms of the wave number spectrum:

$$\zeta(\vec{x}_0, t_0; \vec{x}, t) = \iint_{\vec{k}} A(x_0, t_0; \vec{k}) \exp\{i(\vec{k} \times \vec{x} - \omega t)\} d\vec{k} \qquad (7)$$

where subscript 0 of $\vec{x}_0$, t_0 indicates the slow varying of horizontal space and time, $A(x_0, t_0; \vec{k})$ is the amplitude of wave elevation, $\vec{k}$ and ω are the wave number and frequency, respectively, and $\vec{x} = x\vec{i} + y\vec{j}$.

Inserting Eq. 7 into Eq. 6a and e yields the velocity potential function:

$$\phi(\vec{x}_0, z_0, t_0; \vec{x}, z, t)$$
$$= \iint_{\vec{k}} \Phi(\vec{x}_0, z_0, t_0; \vec{k}) \exp\{kz\} \exp\{i(\vec{k} \times \vec{x} - \omega t)\} d\vec{k} \qquad (8)$$

where $\Phi(\vec{x}_0, z_0, t_0; \vec{k})$ is the amplitudes of velocity potential function with wave number and frequency $\vec{k}$ and ω.

From Eq. 6c and d, we have the wave dispersion relationship:

$$\omega = \sqrt{gk} \qquad (9)$$

and the relationship between wave amplitude and potential amplitude:

$$-i\omega A(\vec{k}) = k\Phi(\vec{k}). \qquad (10)$$

Combining Eqs. 8 and 10 gives:

$$\phi(\vec{x}, z, t) = \iint_{\vec{k}} -i\frac{\omega}{k} A(\vec{k}) \exp\{kz\} \exp\{i(\vec{k} \cdot \vec{x} - \omega t)\} d\vec{k}. \qquad (11)$$

Inserting Eq. 11 into Eq. 6b, we obtain the wave velocities:

$$\{u_{1w}, u_{2w}, u_{3w}\} = \nabla\phi$$

$$= \left\{ \begin{array}{l} \iint_{\vec{k}} \omega \frac{k_x}{k} A(\vec{k}) \exp\{kz\} \exp\{i(\vec{k} \cdot \vec{x} - \omega t)\} d\vec{k} \\ \iint_{\vec{k}} \omega \frac{k_y}{k} A(\vec{k}) \exp\{kz\} \exp\{i(\vec{k} \cdot \vec{x} - \omega t)\} d\vec{k} \\ \iint_{\vec{k}} -i\omega A(\vec{k}) \exp\{kz\} \exp\{i(\vec{k} \cdot \vec{x} - \omega t)\} d\vec{k} \end{array} \right\}. \qquad (12)$$

2.3 The closure of momentum equations of ocean circulation

2.3.1 Wave-induced Reynolds stress

From Eq. 12, one component of the wave-induced Reynolds stress is:

$$\tau_{ww12} = -\langle u_{1w}u_{2w}\rangle = -\text{Re} \iint_{\vec{k}} \iint_{\vec{k}'} \omega\omega' \frac{k_1 k'_2}{kk'} \langle A(\vec{k})A^*(\vec{k}')\rangle$$
$$\exp\{(k+k')z\} \exp\{i[(\vec{k}-\vec{k}') \cdot \vec{x} - (\omega-\omega')t]\} d\vec{k} d\vec{k}'. \qquad (13)$$

Since we assume that the ocean wave is a stationary process, we have:

$$\langle A(\vec{k})A^*(\vec{k}')\rangle = \delta(\vec{k}-\vec{k}')E(\vec{k}) \qquad (14)$$

where $E(\vec{k})$ is the wave number spectrum which can be computed from a third-generation wave number spectrum numerical model (Yuan et al. 1991; Donelan and Yuan 1994; Yang et al. 2005).

Inserting Eq. 14 into Eq. 13 gives:

$$\tau_{ww12} = -\langle u_{1w}u_{2w}\rangle = -\iint_{\vec{k}} \omega^2 \frac{k_1 k_2}{k^2} E(\vec{k}) \exp\{2kz\} d\vec{k}. \qquad (15)$$

Similarly, we can obtain:

$$\tau_{ww11} = -\langle u_{1w}u_{1w}\rangle = -\iint_{\vec{k}} \omega^2 \frac{k_1^2}{k^2} E(\vec{k}) \exp\{2kz\} d\vec{k},$$

$$\tau_{ww22} = -\langle u_{2w}u_{2w}\rangle = -\iint_{\vec{k}} \omega^2 \frac{k_2^2}{k^2} E(\vec{k}) \exp\{2kz\} d\vec{k},$$

$$\tau_{ww33} = -\langle u_{3w}u_{3w}\rangle = -\iint_{\vec{k}} \omega^2 E(\vec{k}) \exp\{2kz\} d\vec{k},$$

$$\tau_{ww13} = -\langle u_{1w}u_{3w}\rangle = -\text{Re} \iint_{\vec{k}} i\omega^2 \frac{k_1}{k} E(\vec{k}) \exp\{2kz\} d\vec{k} = 0,$$

$$\tau_{ww21} = -\langle u_{2w}u_{1w}\rangle = -\iint_{\vec{k}} \omega^2 \frac{k_1 k_2}{k^2} E(\vec{k}) \exp\{2kz\} d\vec{k},$$

$$\tau_{ww31} = -\langle u_{3w}u_{1w}\rangle = 0,$$

$$\tau_{ww23} = -\langle u_{2w}u_{3w}\rangle = 0,$$

$$\tau_{ww32} = -\langle u_{3w}u_{2w}\rangle = 0.$$

Finally, the wave-induced Reynolds stress tensor has the form:

$$\{-\langle u_{iw}u_{jw}\rangle\}$$

$$= \left\{ \begin{array}{ccc} -\iint_{\vec{k}}\frac{k_1^2}{k^2}EE(\vec{k})\mathrm{d}\vec{k} & -\iint_{\vec{k}}\frac{k_1 k_2}{k^2}EE(\vec{k})\mathrm{d}\vec{k} & 0 \\[2mm] -\iint_{\vec{k}}\frac{k_1 k_2}{k^2}EE(\vec{k})\mathrm{d}\vec{k} & -\iint_{\vec{k}}\frac{k_2^2}{k^2}EE(\vec{k})\mathrm{d}\vec{k} & 0 \\[2mm] 0 & 0 & -\iint_{\vec{k}}EE(\vec{k})\mathrm{d}\vec{k} \end{array} \right\}$$

$$(16)$$

where $EE(\vec{k}) = \omega^2 E(\vec{k})\exp\{2kz\}$.

2.3.2 Momentum mixing induced by surface wave motion

We use an analogy to the Prandtl mixing length theory to parameterize the momentum mixing induced by wave motion. Thus, the second and third terms on the right-hand side of Eq. 3, $\tau_{wcij} = -\langle u_{iw}u_{jc}\rangle - \langle u_{ic}u_{jw}\rangle$, are expressed as:

$$\tau_{wc11} = 2B_H\frac{\partial U_1}{\partial x_1}, \quad \tau_{wc22} = 2B_H\frac{\partial U_2}{\partial x_2}, \quad \tau_{wc33} = 2B_V\frac{\partial U_3}{\partial x_3}$$
$$\tau_{wc12} = \tau_{wc21} = B_H\left(\frac{\partial U_1}{\partial x_2} + \frac{\partial U_2}{\partial x_1}\right)$$
$$\tau_{wc13} = \tau_{wc31} = B_H\frac{\partial U_3}{\partial x_1} + B_V\frac{\partial U_1}{\partial x_3}$$
$$\tau_{wc23} = \tau_{wc32} = B_H\frac{\partial U_3}{\partial x_2} + B_V\frac{\partial U_2}{\partial x_3}$$

$$(17)$$

where:

$$\begin{aligned} B_H &= \langle l_{1w}u'_{1w}\rangle = \langle l_{2w}u'_{2w}\rangle \\ B_V &= \langle l_{3w}u'_{3w}\rangle \end{aligned}.$$

$$(18)$$

For ocean surface wave processes, we assume that the mixing length l_{iw} is proportional to the range of the particle displacement in the i-th direction. We need to note that the concern of the expression u'_{iw} here is not the mathematical derivation, but a concept and assumption of equivalent scales. u'_{iw} should be understood as the increment of the wave motion velocity at the spatial interval of l_{iw} in the i-th direction, and so can be expressed as:

$$u'_{iw} = l_{iw}\frac{\partial}{\partial x_i}\langle u_{iw}u_{iw}\rangle^{\frac{1}{2}}.$$

$$(19)$$

For example:

$$u'_{1w} = l_{1w}\frac{\partial}{\partial x_1}\langle u_{1w}u_{1w}\rangle^{\frac{1}{2}}$$
$$= l_{1w}\frac{\partial}{\partial x_1}\left(\iint_{\vec{k}}\omega^2\frac{k_x^2}{k^2}E(\vec{k})\exp\{2kz\}\mathrm{d}\vec{k}\right)^{\frac{1}{2}}.$$

Since ocean waves are locally uniform, the horizontal changes of statistic parameters for ocean waves within the length of l_{iw} is nearby 0. Therefore:

$$u'_{1w} \approx 0, \ u'_{2w} \approx 0.$$

$$(20)$$

But, for the vertical direction:

$$u'_{3w} = l_{3w}\frac{\partial}{\partial z}\left(\iint_{\vec{k}}\omega^2 E(\vec{k})\exp\{2kz\}\mathrm{d}\vec{k}\right)^{\frac{1}{2}}.$$

$$(21)$$

So, we have:

$$B_H = 0,$$

$$(22)$$

$$B_V = \langle l_{3w}^2\rangle\frac{\partial}{\partial x_3}\langle u_{3w}u_{3w}\rangle^{\frac{1}{2}} = \langle l_{3w}^2\rangle\frac{\partial}{\partial z}\left(\iint_{\vec{k}}\omega^2 E(\vec{k})\exp\{2kz\}\mathrm{d}\vec{k}\right)^{\frac{1}{2}}$$

$$(23)$$

where the mixing length l_{3w} is proportional to the wave partial displacement:

$$l_{3w} \sim \iint_{\vec{k}}A(\vec{k})\exp\{kz\}\exp\{i(\vec{k}\cdot\vec{x} - \omega t)\}\mathrm{d}\vec{k}.$$

$$(24)$$

Thus:

$$\langle l_{3w}^2\rangle = \alpha\iint_{\vec{k}}E(\vec{k})\exp\{2kz\}\mathrm{d}\vec{k}$$

$$(25)$$

where $\alpha = O(1)$ is a parameter which should be determined by observations or numerical experiments. If we regard wave amplitude or wave height as the mixing length, α should be 4 or 1, respectively. For the initial test here, we suggest $\alpha = 1$.

Inserting Eq. 25 into Eq. 23 gives:

$$B_V = \alpha\iint_{\vec{k}}E(\vec{k})\exp\{2kz\}\mathrm{d}\vec{k}\ \frac{\partial}{\partial z}\left(\iint_{\vec{k}}\omega^2 E(\vec{k})\exp\{2kz\}\mathrm{d}\vec{k}\right)^{\frac{1}{2}}.$$

$$(26)$$

Wave number spectrum $E(\vec{k})$ is a function of x, y, and t and can be computed by integrating a wave number spectrum numerical model. B_V is a function of x, y, z, and t and is defined as the wave-induced viscosity (or diffusivity).

Finally, we get:

$$\tau_{wcij} = -[\langle u_{iw}u_{jc}\rangle + \langle u_{ic}u_{jw}\rangle]$$

$$= \left\{ \begin{array}{ccc} 0 & 0 & B_V\frac{\partial U_1}{\partial x_3} \\[2mm] 0 & 0 & B_V\frac{\partial U_2}{\partial x_3} \\[2mm] B_V\frac{\partial U_1}{\partial x_3} & B_V\frac{\partial U_2}{\partial x_3} & 2B_V\frac{\partial U_3}{\partial x_3} \end{array} \right\}.$$

$$(27)$$

2.4 The wave-induced mixing for temperature and salinity

In Eqs. 4 and 5, the wave-induced Reynolds fluxes for temperature and salinity, $-\langle u_{iw}\theta\rangle$ and $-\langle u_{iw}s\rangle$, need to be closed.

Similar with the momentum equation, we also follow the Prandtl mixing length theory:

$$-\langle u_{1w}\theta\rangle = B_H \frac{\partial T}{\partial x_1}, \quad -\langle u_{2w}\theta\rangle = B_H \frac{\partial T}{\partial x_2},$$
$$-\langle u_{3w}\theta\rangle = B_V \frac{\partial T}{\partial x_3}, \tag{28}$$

$$-\langle u_{1w}s\rangle = B_H \frac{\partial S}{\partial x_1}, \quad -\langle u_{2w}s\rangle = B_H \frac{\partial S}{\partial x_2},$$
$$-\langle u_{3w}s\rangle = B_V \frac{\partial S}{\partial x_3}. \tag{29}$$

Provided that surface ocean waves are locally uniform, we have:

$$-\langle u_{1w}\theta\rangle \cong -\langle u_{2w}\theta\rangle \cong 0, \quad -\langle u_{3w}\theta\rangle = B_V \frac{\partial T}{\partial x_3}, \tag{30}$$

$$-\langle u_{1w}s\rangle \cong -\langle u_{2w}s\rangle \cong 0, \quad -\langle u_{3w}s\rangle = B_V \frac{\partial S}{\partial x_3}. \tag{31}$$

So:

$$\{-\langle u_{iw}\theta\rangle, -\langle u_{iw}s\rangle\} = \left\{ \begin{array}{cc} 0 & 0 \\ 0 & 0 \\ B_V \frac{\partial T}{\partial z} & B_V \frac{\partial S}{\partial z} \end{array} \right\}. \tag{32}$$

With Eqs. 16, 26, 27, 32, and 1, the governing equations of ocean circulation with surface wave processes incorporated are formulated. It is shown that the wave-induced mixing can be considered in ocean circulation models simply by adding B_V to the viscosity (or diffusivity) coefficient. The three-dimensional wave-induced Reynolds stress can be included in ocean models by Eq. 16. The wave number spectrum $E(\vec{k})$ can be calculated from a third-generation wave number spectrum numerical model.

2.5 The closure of the wave-induced mixing in term of a monochromatic wave

Instead of Eq. 7, if we regard the surface wave as the following monochromatic wave:

$$\zeta = A \exp\{i(\vec{k}\cdot\vec{x} - \omega t)\}, \tag{33}$$

the wave velocity components can be written as:

$$\{u_{1w}, u_{2w}, u_{3w}\}$$
$$= \left\{ \begin{array}{c} \omega\frac{k_1}{k} A \exp\{kx_3\} \exp\{i(k_\alpha x_\alpha - \omega t)\} \\ \omega\frac{k_2}{k} A \exp\{kx_3\} \exp\{i(k_\alpha x_\alpha - \omega t)\} \\ -i\omega\, A \exp\{kx_3\} \exp\{i(k_\alpha x_\alpha - \omega t)\} \end{array} \right\} \tag{34}$$

where A, k, and ω are the amplitude, wave number, and frequency of the monochromatic ocean surface wave, respectively.

Following the idea of the Prandtl mixing length theory, we get:

$$u'_{3w} = l_{3w} \frac{\partial}{\partial x_3} \langle u_{3w}u_{3w}\rangle^{\frac{1}{2}} = l_{3w}\omega\, Ak \exp\{kz\}$$

and

$$B_V = \langle l_{3w}u'_{3w}\rangle = l_{3w}^2 \omega\, Ak \exp\{kz\}. \tag{35}$$

Since the mixing length l_{3w} is proportional to the wave particle displacement:

$$l_{3w} \sim A \exp\{kz\} \exp\{i(\vec{k}\cdot\vec{x} - \omega t)\},$$

so:

$$\langle l_{3w}^2\rangle = \alpha A^2 \exp\{2kz\} \tag{36}$$

where α is a constant which should be determined by observations or numerical experiments. In the present study, it is set to be 1 as above.

At last, we get:

$$B_V = \alpha A^3 k \omega \exp\{3kz\} = \alpha A\, u_s \exp\{3kz\} \tag{37}$$

where $u_s = c(Ak)^2$ is the Stokes drift and $c = \frac{\omega}{k}$ is the phase velocity of surface wave.

2.6 The wave-induced mixing for finite water depth

Instead of Eq. 6, we use:

$$\left|\frac{\partial\phi}{\partial z}\right| = 0 \qquad z = -H \tag{38}$$

where H is the water depth. The wave dispersion relation is:
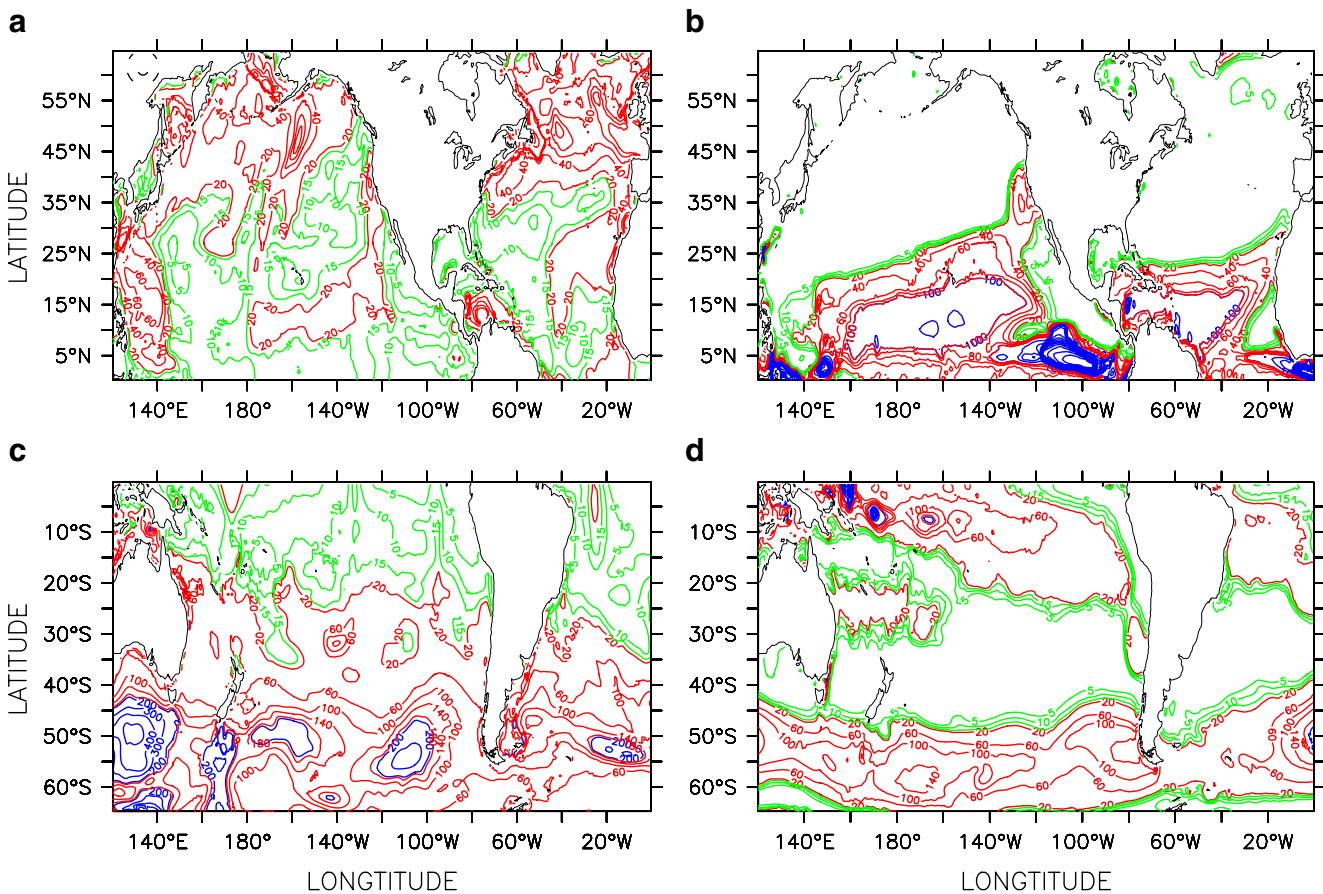
$$\omega^2 = gk \tanh(kH). \tag{39}$$

Fig. 1 The spatial distributions of the upper 20-m averaged B_V and K_{hc} from the M-Y turbulence closure model. **a** B_V in the Northern Hemisphere in July, **b** K_{hc} in the Northern Hemisphere in July, **c** B_V in the Southern Hemisphere in February, and **d** K_{hc} in the Southern Hemisphere in February. For **a** and **b**, contour interval is 5 cm² s⁻¹ from 0 to 20 cm² s⁻¹, 20 cm² s⁻¹ from 20 to 200 cm² s⁻¹, and 100 cm² s⁻¹ from 200 to 2000 cm² s⁻¹; for **c** and **d**, contour interval is 5 cm² s⁻¹ from 0 to 20 cm² s⁻¹, 40 cm² s⁻¹ from 20 to 200 cm² s⁻¹, and 100 cm² s⁻¹ from 200 to 2000 cm² s⁻¹

Fig. 2 Zonally averaged B_V (*solid*, cm² s⁻¹) and K_{hc} (*dashed*, cm² s⁻¹) in Fig. 1 in **a** the North Pacific and Atlantic and **b** the Southern Hemisphere
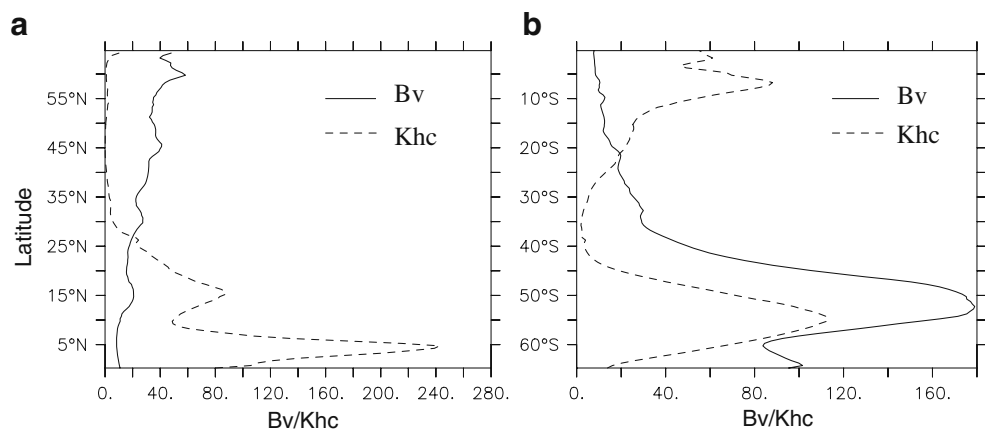
Fig. 3 Profiles of zonally aver-
aged summer B_V (*solid*, cm^2 s^{-1})
and K_{hc} (*dashed*, cm^2 s^{-1}) in the
Pacific and Atlantic (120° E–0°
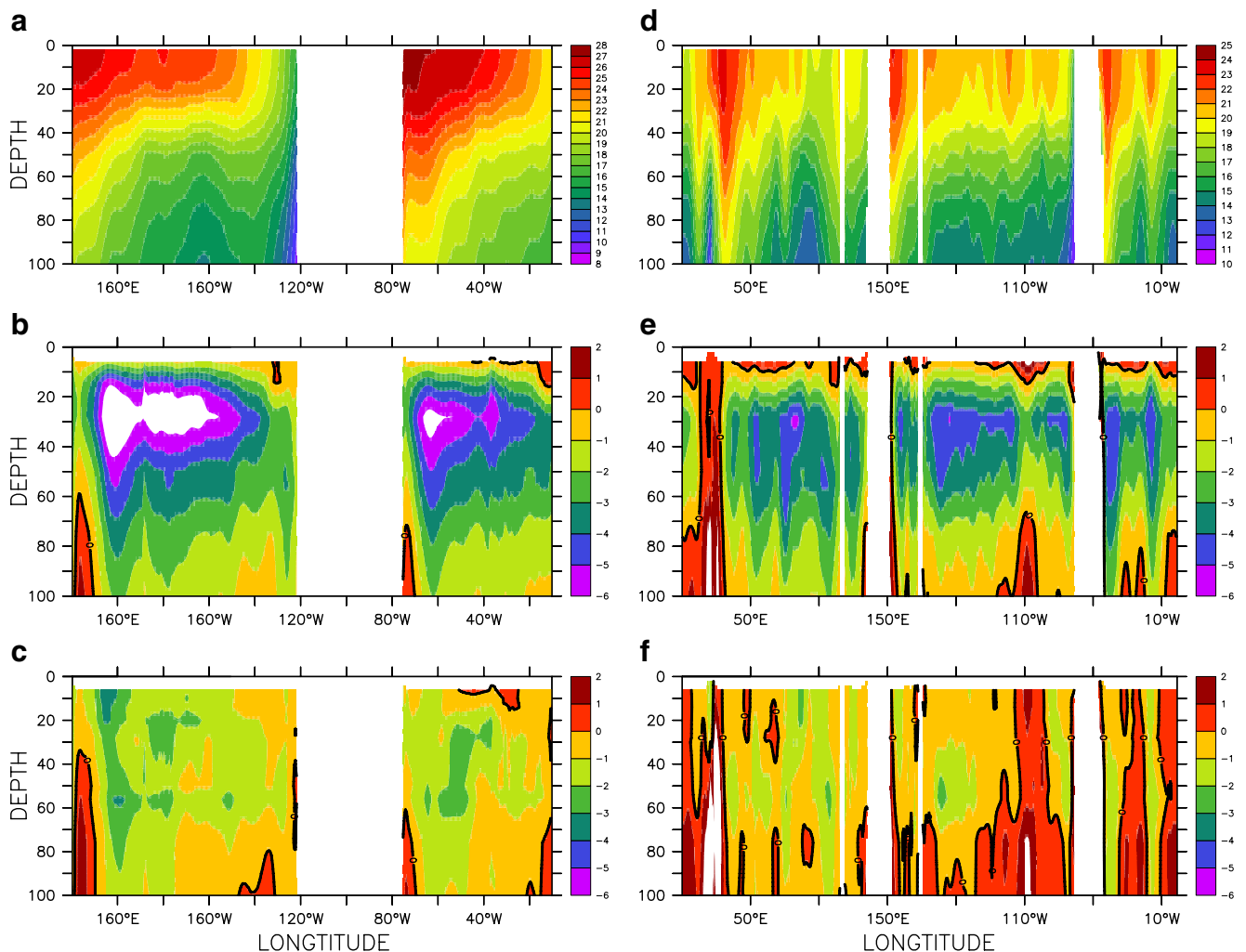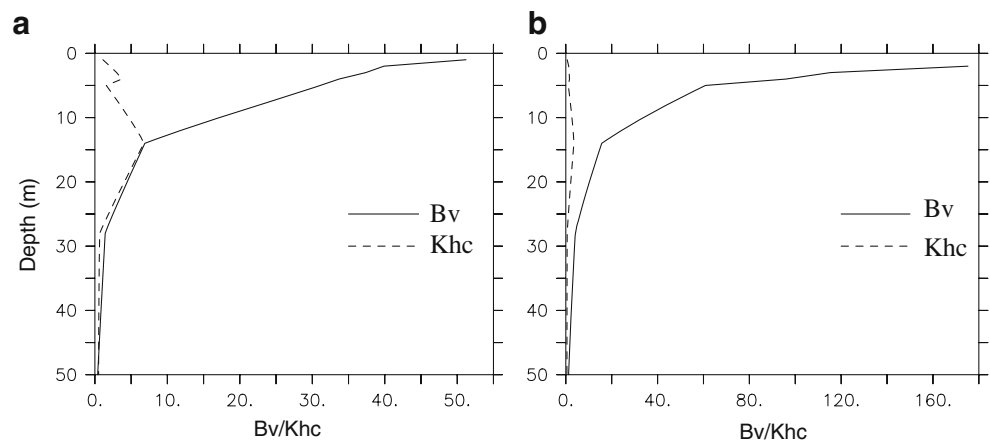W) **a** along 35° N in July and **b**
along 35° S in February

Fig. 4 The *upper panel* shows the temperature distribution of the
Levitus data; the *middle panel* is the temperature difference between
the model calculations without B_V and the Levitus climatology; the
lower panel is the temperature difference between the coupled wave–
circulation model results and the Levitus data. The *left column* is along
35° N in July and the *right column* is along 35° S in February

The wave velocity components for finite water depth can be derived as:

$$\{u_{1w}, u_{2w}, u_{3w}\} = \nabla\phi = \left\{ \begin{array}{l} \iint_{\vec{k}} \frac{\omega k_x}{k} A(\vec{k}) \frac{\cosh k(H+z)}{\sinh kH} \exp\left\{i(\vec{k}\cdot\vec{x} - \omega t)\right\} d\vec{k} \\ \iint_{\vec{k}} \frac{\omega k_y}{k} A(\vec{k}) \frac{\cosh k(H+z)}{\sinh kH} \exp\left\{i(\vec{k}\cdot\vec{x} - \omega t)\right\} d\vec{k} \\ \iint_{\vec{k}} -i\omega A(\vec{k}) \frac{\sinh k(H+z)}{\sinh kH} \exp\left\{i(\vec{k}\cdot\vec{x} - \omega t)\right\} d\vec{k} \end{array} \right\}. \tag{40}$$

In a similar way to that described above, the wave-induced vertical kinematic viscosity (or diffusivity) is derived as:

$$B_V = \alpha \iint_{\vec{k}} E(\vec{k}) \frac{sh^2\{k(H+z)\}}{sh^2\{kH\}} d\vec{k} \frac{\partial}{\partial z} \left[\iint_{\vec{k}} \omega^2 \frac{sh^2\{k(H+z)\}}{sh^2\{kH\}} E(\vec{k}) d\vec{k} \right]^{\frac{1}{2}}. \tag{41a}$$

For monochromatic surface wave in finite water depth:

$$B_V = \alpha A^3 k\omega \left[\frac{\sinh k(H+z)}{\sinh kH} \right]^3 = \alpha A u_s \left[\frac{\sinh k(H+z)}{\sinh kH} \right]^3. \tag{41b}$$

2.7 The wave number spectrum numerical model

In order to get $E(\vec{k})$, the marine science and numerical modeling (MASNUM) wave number spectral model is adopted. This wave numerical model was first developed by Yuan et al. (1991). It has been validated many times by observations (e.g., Yu et al. 1997) and applied in ocean engineering in China (Qiao et al. 1999). Recently, it was expanded into the global ocean with spherical coordinates by Yang et al. (2005) and is used in this paper to compute the wave number spectrum, which is necessary for computing the wave-induced viscosity (or diffusivity), B_V, in Eq. 26 or 41a.

The computational domain is (78° S–65° N, 0°–360° E) with a horizontal resolution of 0.5° by 0.5° and a time step of 30 min from 1 Jan. 2001 to 31 Dec. 2001. The National Centers for Environmental Prediction reanalyzed wind fields with the horizontal resolution of 1.25° by 1.0° and time interval of 6 h interpolated into the model grid are used. From Yang et al. (2005), the wave model results agree with altimetry data reasonably well. Although current has some effects on surface wave through wave–current interaction source function, this kind of effect can be neglected except in high wind speed such as typhoon or hurricane cases.

3 Model results

In order to evaluate the effects of the wave-induced vertical mixing, B_V, we first test the wave-induced mixing scheme

by employing POM (Blumberg and Mellor 1987). Note that the scheme has been implemented also in other community ocean models, including the Regional Ocean Model System (ROMS; Haidvogel et al. 2000) and the Hallberg Isopycnal Model; the impact of the wave-induced mixing improved their performance in a similar manner to the POM test here, and the results will be presented in separate papers. The simulation area is (78° S–65° N, 0°–360° E) with solid boundary in the north. While the exchanges of water and heat at 65° N between the Arctic Ocean and the Atlantic Ocean are important for climate simulations, in the context of the upper ocean mixing tests discussed here, the simulation results should not be affected by this limitation, especially for the region far away from the north boundary areas. The horizontal resolution of POM is 0.5° by 0.5°. The vertical sigma grids have the following 16 sigma levels with a fine resolution in the upper layers (0.000, −0.003, −0.006, −0.013,
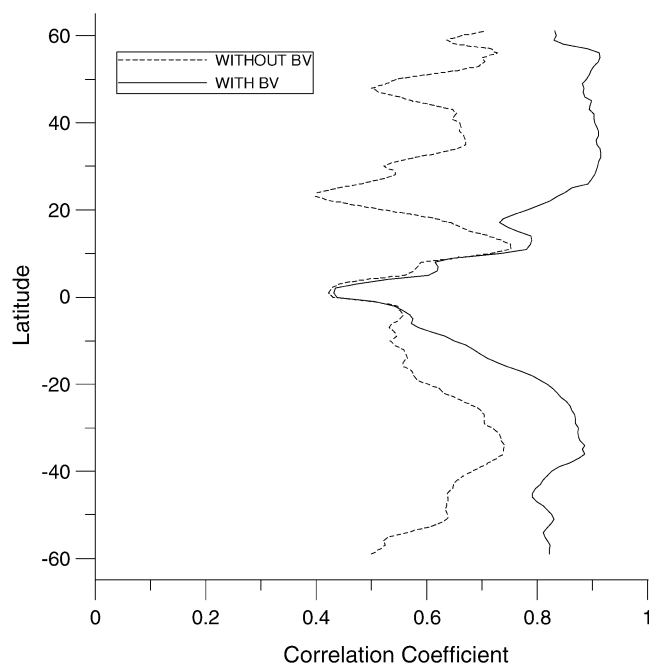

Fig. 5 Longitudinal distributions of zonally averaged correlation coefficient between simulated temperature and Levitus data in the upper 100-m ocean. *Solid* and *dashed lines* denote results from coupled POM and uncoupled POM, respectively

−0.025, −0.050, −0.100, −0.200, −0.300, −0.400, −0.500, −0.600, −0.700, −0.800, −0.900, −1.00). The model topography is interpolated from the global 5′ by 5′ ETOPO5 dataset. As this paper focuses on the upper oceans, the maximal water depth is set to 3,000 m in order to improve the vertical resolution at a reasonable cost.

The climatological sea surface wind stress and heat flux (Q) are from the Comprehensive Ocean–Atmosphere Data Set (COADS; da Silva et al. 1994a, b). Q is modified by using the Haney equation (Haney 1971):

$$Q = Q_c + \left(\frac{dQ}{dT}\right)_c \left(T_c^0 - T^0\right) \tag{42}$$

where the subscript c means data from COADS and T^0 is the SST from the circulation model.

The wave-induced vertical mixing can be included directly as follows:

$$K_m = K_{mc} + B_V, \quad K_h = K_{hc} + B_V \tag{43}$$

where K_m and K_h are the vertical viscosity and diffusivity used in the circulation model, respectively, K_{mc} and K_{hc} are calculated by the M-Y scheme (Mellor and Yamada 1982), and B_V is the additional term obtained from the MASNUM wave number spectrum numerical model, which is saved every 2 days averaged and coupled with the circulation model with a linear interpolation to each time step.

The initial conditions of temperature and salinity in January are from the Levitus (1982) dataset, and the initial velocity is set as 0. After a 5-year computation for spin up,
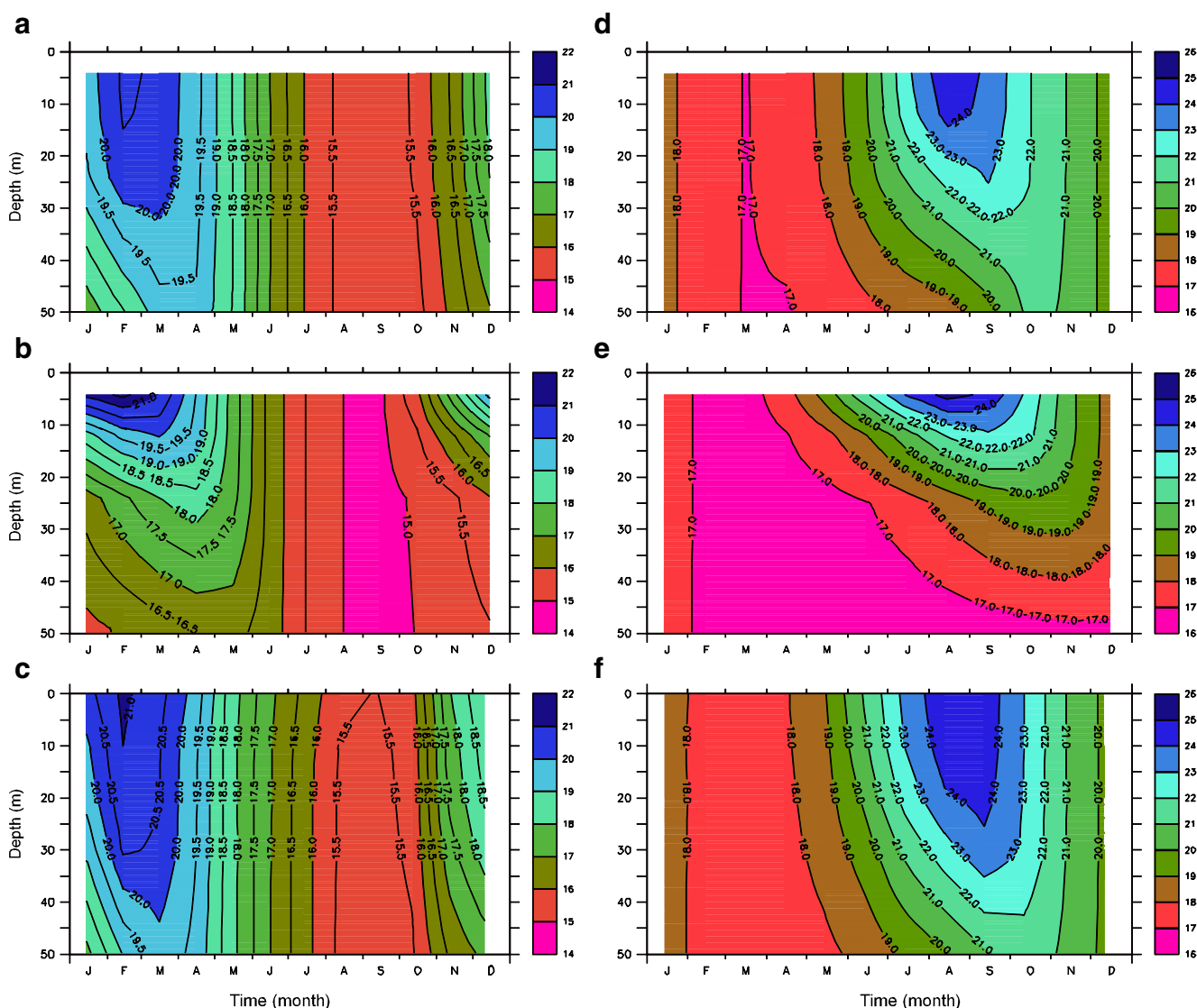

Fig. 6 The time evolutions of the upper 50-m temperature at (35° S, 180° E) (*left column*) and (35° N, 30° W) (*right column*) with the wave-induced mixing (*upper*), without the wave-induced mixing (*middle*), and from the Levitus data (*lower*)

the model has reached a stable condition under which the total kinetic energy have an annual cycle without obvious drifts. Then, the model results of the sixth year are used for the following analysis.

### 3.1 The distributions of wave-induced viscosity/diffusivity

The left column of Fig. 1 shows the distribution of the upper 20-m averaged B_V (monthly averaged) in summer in which July is selected to represent the Northern Hemisphere (Fig. 1a) and February for the Southern Hemisphere (Fig. 1c). For comparisons, the vertical diffusivity from the M-Y turbulence closure model is shown in the right column (Fig. 1b, d).

In the Northern Hemisphere, the upper 20-m averaged B_V is higher to the north of 30° N than that between 0° and 30° N. In the north Pacific, there are two high-value centers of 60 and 100 cm^2 s^{-1} at (15° N, 140° E) and (45° N, 160° W), respectively. In the North Atlantic, two high-value centers of 140 and 100 cm^2 s^{-1} appear around (45° N, 70° W) and (48° N, 15° W), respectively. The vertical diffusivity, K_{hc}, from the M-Y turbulence closure model shows a much different pattern (Fig. 1b). In the north of 25° N, K_{hc} is <5 cm^2 s^{-1} with most of the area <1 cm^2 s^{-1}, which means K_{hc} is much less than B_V. The wave-induced mixing plays a control role in the upper ocean at high latitudes of the Northern Hemisphere in summer. In the north tropical area of 0°–25° N, K_{hc} can reach more than

100 cm^2 s^{-1} in most areas and two high-value centers of 140 and 100 cm^2 s^{-1} appear at (5° N, 100° W) and (2° N, 5° W), respectively. Although the upper 20-m averaged K_{hc} is higher than that of B_V, K_{hc} is 0 at the surface because the mixing length is 0 (Ezer 2000), so B_V will act as a trigger to transmit the surface momentum and energy downward. Thus, B_V still have much influence on the upper ocean. The reason for different spatial distributions of K_{hc} and B_V is as follows. In the area north of 30° N with strong wind stress, B_V is quite large. From the M-Y scheme, $K_{hc}=qlS_H$ where $q^2/2$ is the turbulence kinetic energy and S_H is a stability function associated with the Richardson number (Blumberg and Mellor 1987). S_H is much smaller in the middle and high latitudes than those in the tropical area due to stable stratification; the meridional distribution of the mixing length scale, l, is relatively even. K_{hc} keeps 0 at the sea surface because of the surface boundary condition of $l(0)=0$. So, K_{hc} is very small in the area north of 30° N, showing large meridional variation, while B_V is large due to strong surface waves in this zone.

In February, summer of the Southern Hemisphere, the upper 20-m averaged B_V is <20 cm^2 s^{-1} in southern tropical area (0°–25° S) and is higher as the latitude increases (Fig. 1c) and can reach to more than 400 cm^2 s^{-1} at 55° S. The upper 20-m averaged K_{hc} is higher in the southern tropics than averaged B_V, but much lower in the midlatitude zone of 25–45° S than that of B_V. Although the 20-m averaged K_{hc}

Fig. 7 Comparisons among the simulated temperature (°C) from the uncoupled (dashed) and coupled (dotted) POM and the Levitus data (solid) at (35° S, 180° E) in **a** February, **b** May, **c** August, and **d** November
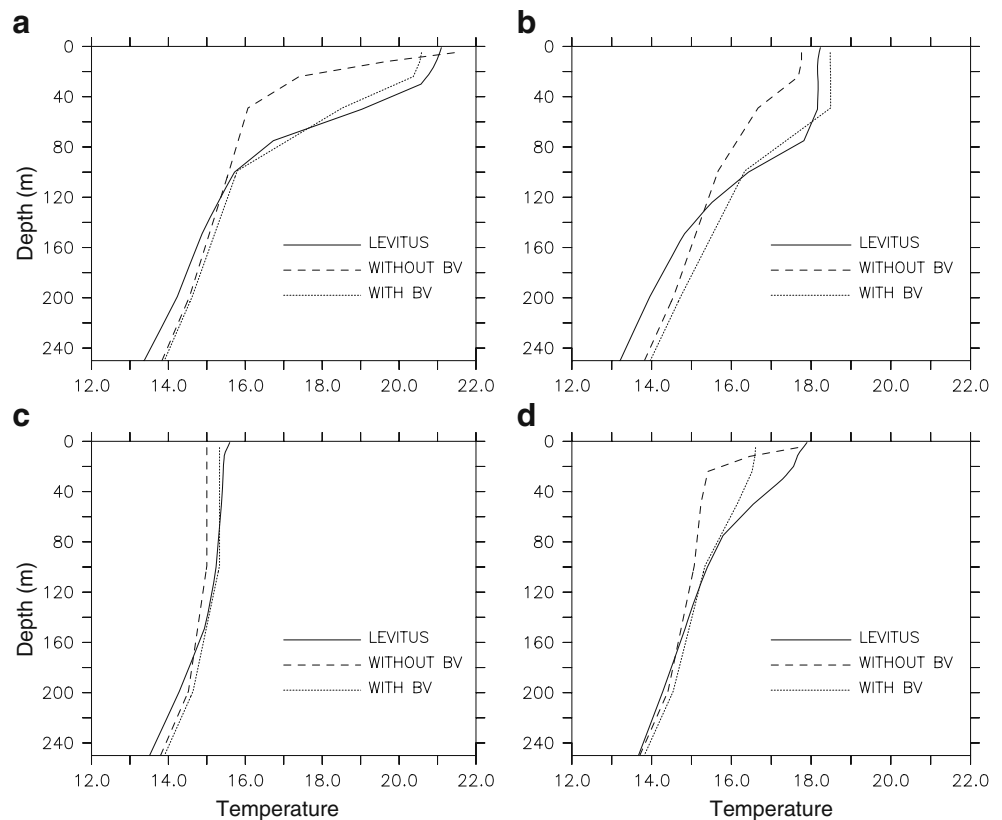
increases rapidly beyond 45° S (Fig. 1d), the averaged B_V is competitive with K_{hc} or higher, especially near the surface.

Figure 2 shows the zonally averaged B_V and K_{hc} calculated from Fig. 1. In the Northern Hemisphere, K_{hc} has two dominant peaks near 5° and 15° N and decrease sharply to high latitudes. At 27° N or so, K_{hc} and B_V are comparable. At higher latitudes, B_V is the dominant factor of vertical mixing in the upper ocean. In the Southern Hemisphere, K_{hc} has two noticeable peaks located near 7° and 55° S. From 40° S to higher latitudes, K_{hc} increase to over 110 cm^2 s^{-1}. At 22° S, K_{hc} and B_V are comparable, but for southern latitudes, B_V exceeds K_{hc}.

In order to show the basin-scale vertical structure of the summer wave-induced viscosity (or diffusivity) B_V and K_{hc} (Km_C) calculated from the M-Y scheme, we compute the vertical profiles of zonally averaged B_V and K_{hc} in the Pacific and Atlantic (120° E–0° W) along 35° N in July (Fig. 3a) and along 35° S in February (Fig. 3b). Qiao et al. (2004a) defined D_5, the depth at which B_V decreases to 5 cm^2 s^{-1}, as the wave-induced mixing penetration depth. Both along 35° N and 35° S, zonally averaged B_V decreases with depth, and averaged D_5 reaches about 20 and 25 m along 35° N and 35° S, respectively. Compared with that, K_{hc} is so weak, especially in the upper ocean. The wave-induced mixing, B_V, controls the mixing processes of the upper ocean in these areas.

3.2 The effect of B_V on the simulation of the temperature structure

Figure 4 shows a comparison between the Levitus data and numerical simulations (with and without B_V) along 35° N in July and along 35° S in February. Transects of the left column cross the Pacific and Atlantic Oceans in which the land is removed to zoom in. The Levitus data are regarded as observations. Without B_V, the simulated temperature shows a large difference, of over 5°C at some locations, between the model and observed climatology (Fig. 4b, e) in summer of both hemispheres. In contrast, the simulated vertical temperature structure with B_V (Fig. 4c, f) is quite close to the Levitus observation (Fig. 4a, d) with much smaller differences. The correlation coefficients are calculated to assess the seasonal variability of temperature (Fig. 5). Along 35° N, the upper 100-m transect–mean correlation coefficient increases to 0.93 with B_V from 0.68 without B_V. The model improvement by B_V shows distinct latitudinal distribution (Fig. 5). In the tropical area, the effects of B_V are trivial, but the correlation between observation and modeling is substantially enhanced toward the poles by incorporating the wave-induced mixing into the model. Obviously, such characteristics are due to the distribution of wave height. Figure 5 is plotted after twofold averaging: the correlation coefficients of the temperature

Fig. 8 Comparisons among the simulated temperature from the uncoupled (*dashed*) and coupled (*dotted*) POM and the Levitus data (*solid*) at (35° N, 30° W) in **a** February, **b** May, **c** August, and **d** November
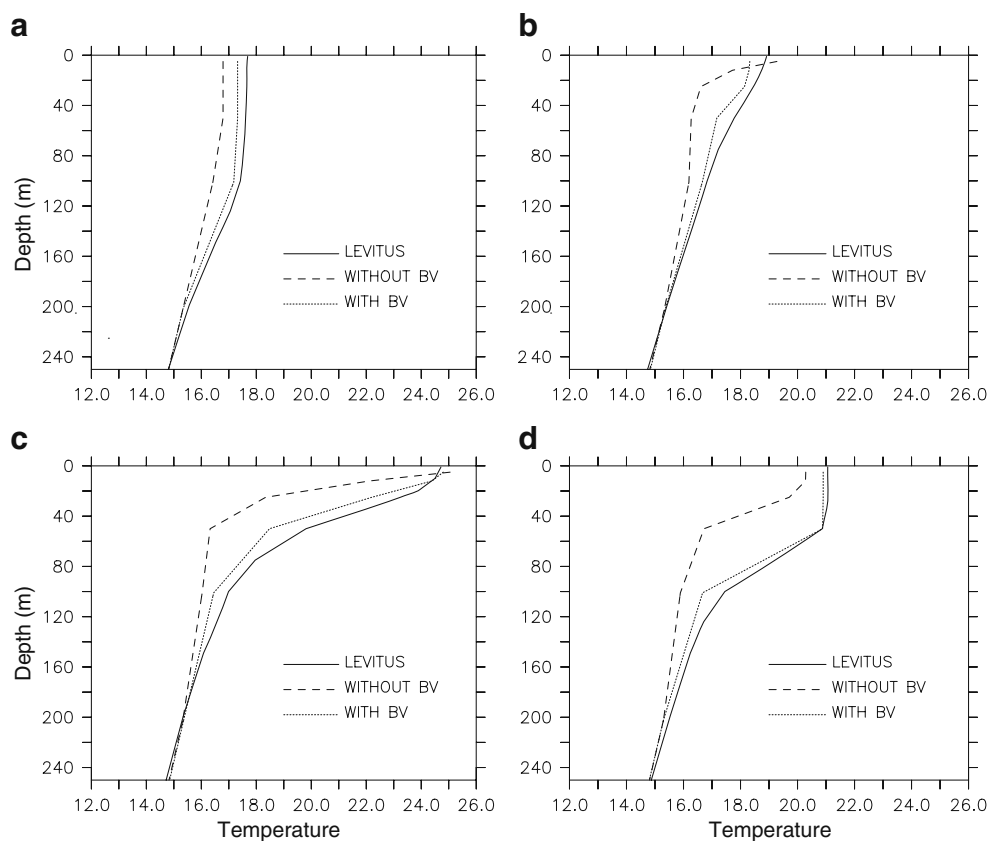
fields have been averaged both zonally along the whole latitude circles and vertically from sea surface to 100-m depth. Therefore, B_V brings about global, rather than local, improvements in modeling the upper ocean thermal structure especially in middle and high latitudes.

The evolution of the two temperature profiles of (35° S, 180° E) and (35° N, 30° W) are selected as the representatives of the South Pacific and North Atlantic basins. At (35° S, 180° E) in the south Pacific, the simulated temperature with B_V (Fig. 6a) is much closer to observation than that without B_V (Fig. 6b), which is obviously higher than the observations (Fig. 6c) at the surface. In Fig. 6b, SST higher than 21°C appears from the early January to the end of March, and the ML is too shallow, the same as mentioned by Martin (1985) and Ezer (2000). For the evolution of the profile at (35° N, 30° W) in the North Atlantic, the simulated SST with B_V in summer is

24°C and last for 1.5 months from early August to mid-September (Fig. 6d). That is similar with the observed SST of which the 24°C isotherm lasts for a little less than 2 months (Fig. 6f). While in the simulation without B_V, the summer SST reaches 25°C, with the period of SST higher than 24°C lasting nearly 3 months, and the thermocline is clearly too shallow (Fig. 6e). One can clearly find that the wave-induced mixing makes the simulated vertical temperature structure (Fig. 6d) much more similar to that observed (Fig. 6f).

The simulated temperature profiles in four seasons are compared with the Levitus data in Fig. 7. In the summer Southern Hemisphere, the simulated SST without B_V is too high and the depth of ML is too shallow in comparison with the Levitus data (Fig. 7a). With B_V, the simulation can rebuild the main feature of the temperature profiles (Fig. 7a–c) except for November (Fig. 7d), spring of the
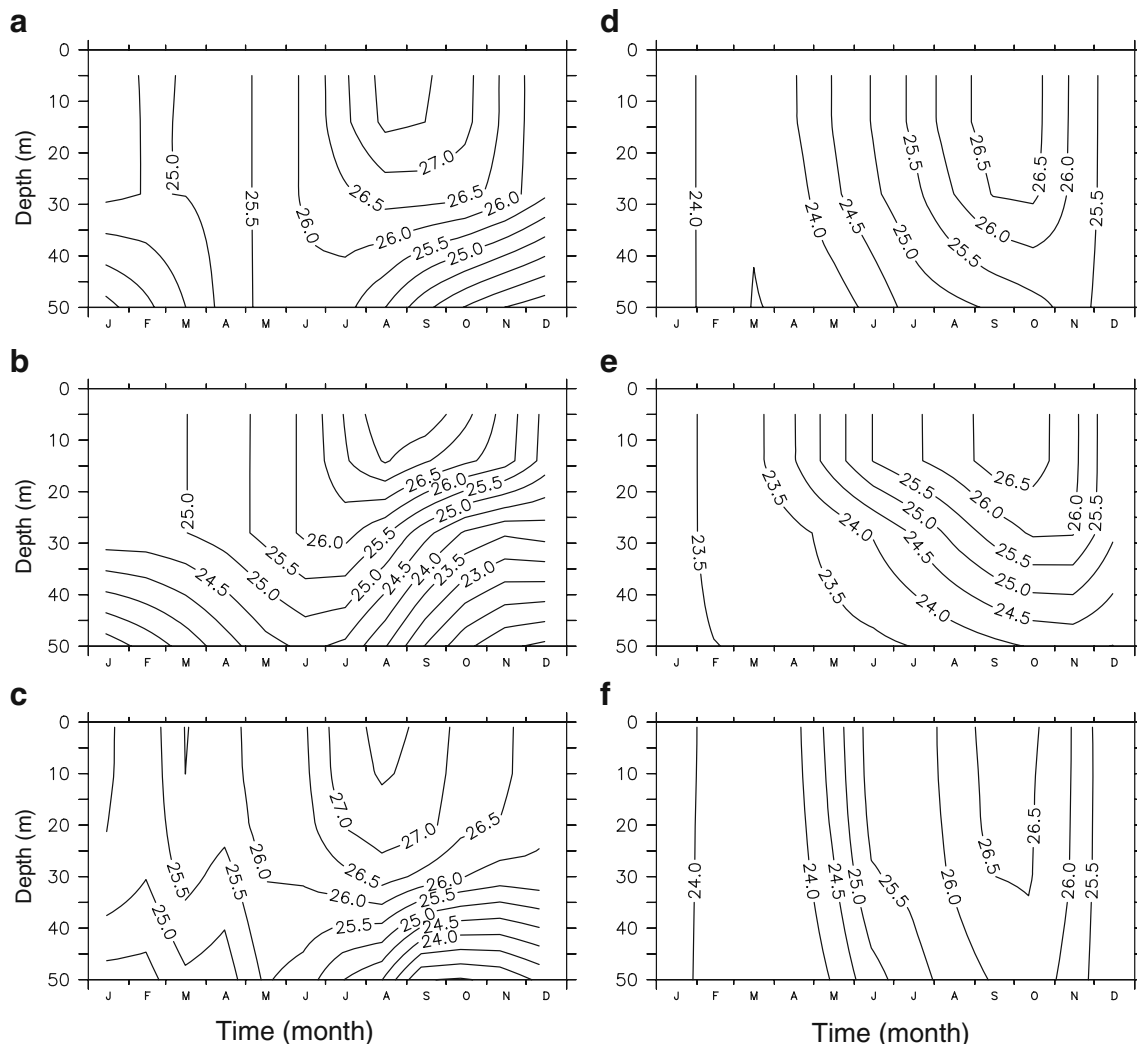

Fig. 9 The time evolutions of the upper 50-m temperature at (15° N, 120° W) (*left column*) and (20° N, 40° W) (*right column*) with the wave-induced mixing (*upper*), without the wave-induced mixing (*middle*), and from the Levitus data (*lower*)

south Pacific. The temperature simulation of the North Atlantic (Fig. 8) shows similar results.

From Fig. 2, we note that, at low latitudes, B_V is much weaker than K_{hc}, especially in the Northern Hemisphere. In order to show that the wave-induced mixing can still affect the vertical temperature structure in tropical areas, two profiles are selected (Fig. 9). The left column of Fig. 9 is the evolution profile at (15° N, 120° W) located in eastern tropical Pacific, the points located in the middle and western tropical Pacific show the same tendency (not shown). The simulated isotherm of 26.5°C with B_V reaches 31 m in August (Fig. 9a), which is similar with the results from Levitus, 32 m (Fig. 9c), while the simulated depth without B_V is only 22 m (Fig. 9b), and

the duration of SST over 27.5°C is 1.1, 1.4, and more than 2.0 months for the Levitus data, with and without B_V, respectively. The comparisons among simulations with and without B_V and Levitus data at the middle tropical Atlantic of (20° N, 40° W) show similar tendency (right column of Fig. 9).

3.3 The effect of B_V on the simulation of ML

ML is an important characteristic parameter for both ocean and atmosphere. Unfortunately, the general ocean circulation model cannot reconstruct the main feature of the observation, i.e., the simulated ML depth is too shallow in summer. Similar to the study of Ezer (2000), we transform the simulated
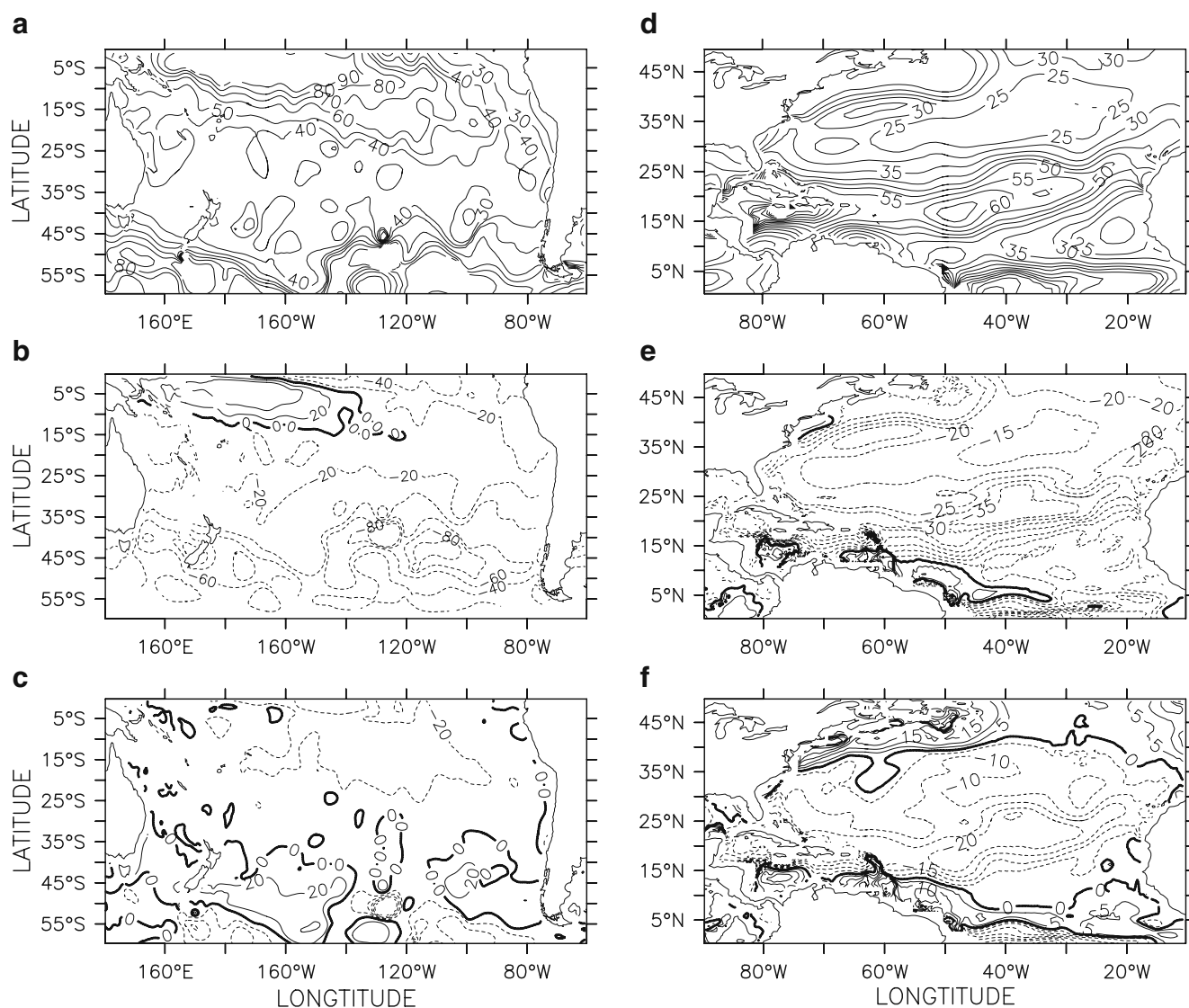

Fig. 10 Results of ML depth (defined as the depth where the temperature differs from the SST by 1°C). The *upper panel* shows the distribution of ML depth from the Levitus data; the *middle panel* shows the differences between modeling without B_V and Levitus data;

the *lower panel* shows the differences between modeling results with B_V and Levitus data. The *left column* is for the South Pacific in February and the *right column* is for the North Atlantic in August

Fig. 11 Zonally averaged ML depth simulated by POM with the wave-induced mixing (*dashed*), without the wave-induced mixing (*dotted*), and from the Levitus data (*solid*) **a** in the South Pacific in February and **b** in the North Atlantic in August
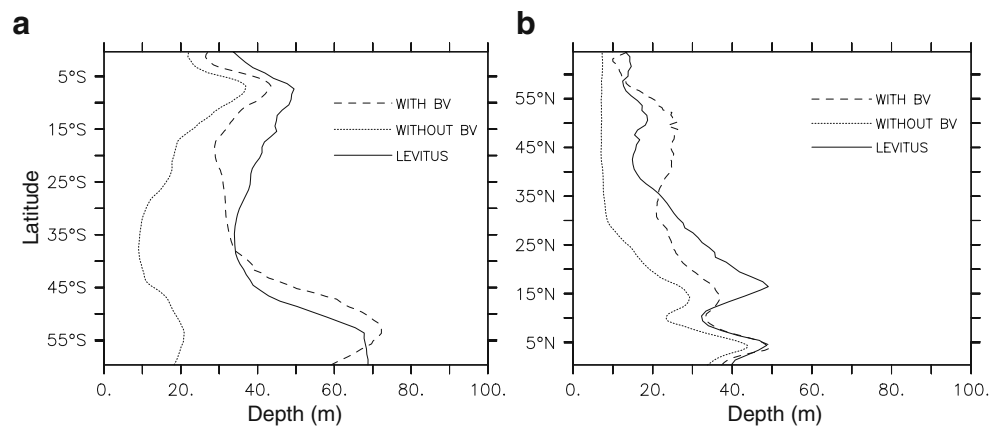
temperature profiles from the sigma grid to high-resolution z levels and calculate the ML depth at each horizontal model grid by searching for the depth where temperature differs from the SST by 1°C. The same definition is adopted for the Levitus (1982) dataset. In general, the ML is the shallowest in summer; we chose February and August to represent summers of the South Pacific (left column of Fig. 10) and North Atlantic (right column of Fig. 10) Oceans, respectively. Figure 11 shows the zonal average of parameters in Fig. 10. For clarity, basins are shown in Fig.10 instead of the whole hemisphere or globe.

In February, summer of the South Pacific, the ML depth of the Levitus data is large in the tropical zone of 0°–20° S and at high latitudes to the south of 45° S (Fig. 10a). Without B_V (Fig. 10b), there is a high-value center of ML depth difference in the tropical area, the averaged depth is more than 10 m shallower than that of Levitus, and the difference generally increases with latitude. For example, the differences are more than 45 m near 55° S. On the contrary, distribution of the simulated ML depth with B_V (Fig. 10c) has much more similar pattern to the observations. In general, the simulated ML depth with B_V is shallower at latitudes lower than 38° S and deeper at latitudes between 38° and 56° S (Fig. 11a).

In August, summer of the Northern Atlantic, besides the high-value zone centered in 5° N, there is a basin-scaled region near the subtropics where the ML is quite deep (Fig. 10d). The simulated results with B_V (Fig. 10f) can reconstruct the main characteristics of the ML depth from the Levitus climatology. Without B_V, the simulated ML depth is shallower than that of Levitus almost everywhere (Figs. 10e and 11b).

3.4 The wave-induced Reynolds stress and wave-driven circulation

McWilliams and Restrepo (1999) mentioned that the surface waves contribute to the slow-time dynamics via the Stokes drift and wave-averaged modifications to the

boundary conditions. We now look at the potential impact that wave-induced stress may have on oceanic transports through the Reynolds stress contribution (Eq. 16).

Let:

$$\vec{\tau_w} = \tau_{w-x_1}\vec{i} + \tau_{w-x_2}\vec{j}$$

$$\tau_{w-x_1} = \frac{\partial \tau_{ww11}}{\partial x_1} + \frac{\partial \tau_{ww12}}{\partial x_2}, \quad \tau_{w-x_2} = \frac{\partial \tau_{ww12}}{\partial x_1} + \frac{\partial \tau_{ww22}}{\partial x_2}.$$

Because the surface gravity waves mainly affect the upper ocean, we run a barotropic mode of the POM with the maximum water depth of 200 m for improving vertical resolution, forced by the daily averaged 3-D wave-induced Reynolds stress $\bar{\tau}_w$ which is calculated from the MASNUM wave number spectrum numerical mode. The stream function (associated with wave-only stress) shows what seems like an eddy field with variations of 500–1000 km scales and ~0.5 Sv amplitudes over the upper 200 m as shown in July (Fig. 12, only the northwest Pacific is shown for a zoom-in view). This result suggests that the additional convergence/divergence in the surface stress field associated with wave-related stresses may add to oceanic eddy variability. However, how to separate the wave-induced
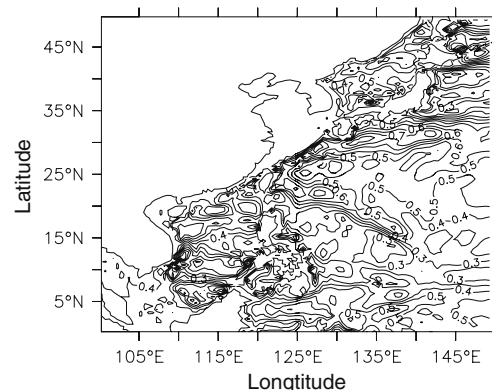
Fig. 12 The stream function (in sverdrup) of wave-driven-only circulation in the Northwest Pacific in July

circulation from field observations remains to be further explored.

4 Discussion and conclusions

In this paper, the surface wave-induced velocity fluctuations are considered in closing the Reynolds stress and fluxes terms of the governing equations for ocean circulation equations. Based on this approach, we proposed a way which allows considering the contribution of surface gravity waves to ocean general circulation models by including the wave-induced Reynolds stresses and wave-induced vertical mixing B_V (viscosity and diffusivity). The expressions of B_V is derived as functions of the Stokes drift for a monochromatic wave and the wave number spectrum in the cases of infinite ("deep-water waves") and finite ("shallow-water waves") water depth, respectively. B_V is the key factor for the wave–circulation coupled processes; its impact may dominate the mixing of the upper 100 m in middle and high latitudes. In tropical areas, the effect of B_V on the upper ocean mixing is important, but not as dominant compared with shear-produced turbulence. Note, however, that preliminary experiments with ocean–atmosphere coupled general circulation model with the additional B_V mixing (not shown) reveal a significant improvement in the common problem of tropical biases (Song et al. 2007); further research is needed in this area.

In comparison with the diffusivity coefficient calculated by the M-Y scheme in the POM, K_{hc}, in summer, the surface wave-induced mixing, B_V, shows its importance in middle and high latitudes in the Northern and Southern Hemispheres where K_{hc} is quite small. So, in a global non-eddy-resolving ocean circulation model of POM, simulation of the upper ML and seasonal thermocline in these regions is greatly improved by including the wave-induced mixing. The transect–mean correlation coefficient along 35° N increases from 0.68 without B_V to 0.93 with B_V. Even in low latitudes where B_V is much weaker than K_{hc}, it can also improve the upper thermal structure simulation. The simulated ML depth is much more similar to the observations by including B_V.

We also test the wave-induced mixing relative to another popular mixing scheme, the KPP (Large et al. 1994) in ROMS. Simulations of ML depth by ROMS (not shown) are similar to those of POM (Fig. 10). Note that, unlike the M-Y scheme that was originally developed for high-resolution small-scale problems (and may require sufficiently small grid size), the KPP scheme is more commonly used for large-scale problems with coarse model resolution.

We have to emphasize that the exact mechanism of wave–turbulence interactions are far from being understood, so the proposed methodology and, in particular, the assumption of correlations between wave-induced motions and shear-induced turbulent velocities, need further support and calibration based on theoretical studies, laboratory experiments, and field observations. The direct measurements of nonbreaking wave-induced turbulence by Babanin and Haus (2009) are consistent with the idea of the present paper. The conclusion that surface wave-induced mixing plays an importance role in temperature simulation from Jacobs (1978) gave us more confidence. More important, the preliminary tests with the POM ocean model indicate that the proposed wave-induced parameterization clearly works to improve ocean simulations and eradicate known problems in modeling surface processes and ML dynamics. Additional improvements of the representation of mixing in ocean models due to processes such as surface wave breaking and internal waves also need further attention.

References

Ardhuin F, Jenkins AD (2006) On the interaction of surface waves and upper ocean turbulence. J Phys Oceanogr 36:551–557

Anis A, Moum JN (1995) Surface wave–turbulence interactions: scaling $\varepsilon(z)$ near the sea surface. J Phys Oceanogr 25:2025–2045

Babanin AV (2006) On a wave-induced turbulence and a wave-mixed upper ocean layer. Geophys Res Lett 33:L20605. doi:10.1029/2006GL027308

Babanin AV, Haus BK (2009) On the existence of water turbulence induced by non-breaking surface waves. J Phys Oceanogr 39(10):2675–2679. doi:10.1175/2009JPO4202.1

Blumberg AF, Mellor GL (1987) A description of a three-dimensional coastal ocean circulation model. In: Heaps NS (ed) Three-dimensional coastal ocean models, vol 4. American Geophysical Union, Washington, pp 1–16

Burchard H (2001) Simulating waves-enhanced layer under breaking surface waves with two-equation turbulence models. J Phys Oceanogr 31:3133–3145

Craig PD, Banner ML (1994) Modeling wave-enhanced turbulence in the ocean surface layer. J Phys Oceanogr 24:2546–2559

da Silva AM, Young CC, Levitus S (1994a) Atlas of surface marine data 1994, volume 3, anomalies of heat and momentum fluxes, NOAA Atlas NESDIS 8. US Department of Commerce, NOAA, NESDIS, 411

da Silva AM, Young CC, Levitus S (1994b) Atlas of surface marine data 1994, volume 4, anomalies of fresh water fluxes, NOAA Atlas NESDIS 9. US Department of Commerce, NOAA, NESDIS, 308

Donelan M, Yuan Y (1994) Wave dissipation by surface processes. In: Komen GJ, Cavaleri L, Donelan M et al (eds) Dynamics and modelling of ocean waves. Cambridge University Press, Cambridge, pp 143–155

Ezer T (2000) On the seasonal mixed layer simulated by a basin-scale ocean model and the Mellor–Yamada turbulence scheme. J Geophys Res 105(C7):16843–16855

Haidvogel DB, Arango H, Hedstrom K, Beckmann A, Malanotte-Rizzoli P, Shchepetkin AF (2000) Model evaluation experiments

in the North Atlantic basin: simulations in non-linear terrain-following coordinates. Dyn Atmos Oceans 32:239–282

Haney R (1971) Surface thermal boundary condition for ocean circulation models. J Phys Oceanogr 1:241–248

Huang C, Qiao F (2010) Wave–turbulence interaction and its induced mixing in the upper ocean. J Geophys Res 115:C04026. doi:10.1029/2009JC005853

Jacobs CA (1978) Numerical simulation of the natural variability in water temperature during BOMEX using alternative forms of the vertical eddy exchange coefficients. J Phys Oceanogr 8:119–141

Kantha LH, Clayson CA (1994) An improved mixed layer model for geophysical applications. J Geophys Res 99:25235–25266

Kantha LH, Clayson CA (2004) On the effect of surface gravity waves on the mixing in the oceanic mixed layer. Ocean Model 6:101–124

Large WG, McWilliams JC, Doney SC (1994) Oceanic vertical mixing: a review and a model with a nonlocal boundary layer parameterization. Rev Geophys 32:363–403

Levitus S (1982) Climatological atlas of the world ocean. NOAA Prof. Paper No. 13, US Government Printing Office, 173

Lin X, Xie S-P, Chen X, Xu L (2006) A well-mixed warm water column in the central Bohai Sea in summer: effects of tidal and surface wave mixing. J Geophys Res 111:C11017. doi:10.1029/2006JC003504

Lü X, Qiao F, Xia C, Zhu J, Yuan Y (2006) Upwelling off Yangtze River estuary in summer. J Geophys Res 111:C11S08. doi:10.1029/2005JC003250

Malcherek A (2003) A consistent derivation of the wave–energy equation from basic hydrodynamic principles. Ocean Dyn 53:302–308

Martin PJ (1985) Simulation of the mixed layer at OWS November and Papa with several models. J Geophys Res 90:581–597

Matsumo T, Lee JS, Shimizu M, Kim SH, Pang IC (2006) Measurements of the turbulent energy dissipation rate ε and an evaluation of the dispersion process of the Changjiang Diluted Water in the East China Sea. J Geophys Res 111:C11S09. doi:10.1029/2005JC003196

McWilliams JC, Restrepo JM (1999) The wave-driven ocean circulation. J Phys Oceanogr 29:2523–2540

Mellor GL (2001) One dimensional, ocean surface layer modeling: a problem and a solution. J Phys Oceanogr 31:790–809

Mellor GL (2003) The three-dimensional current and wave equations. J Phys Oceanogr 33:1978–1989

Mellor GL (2008) The three dimensional, current and surface wave equations: a revision. J Phys Oceanogr 38:2587–2596

Mellor GL, Blumberg AF (2004) Wave breaking and ocean surface layer thermal response. J Phys Oceanogr 34:693–698

Mellor GL, Yamada T (1982) Development of a turbulence closure model for geophysical fluid problems. Rev Geophys Space Phys 20:851–875

Phillips OM (1961) A note on the turbulence generated by gravity waves. J Geophys Res 66:2889–2893. doi:10.1029/JZ066i009p02889

Qiao F et al (1999) The study of wind, wave, current extreme parameters and climatic characters of the South China Sea. Mar Technol Soc J 33(1):61–68

Qiao F, Yuan Y, Yang Y, Zheng Q, Xia C, Ma J (2004a) Wave-induced mixing in the upper ocean: distribution and application in a global ocean circulation model. Geophys Res Lett 31:L11303. doi:10.1029/2004GL019824

Qiao F, Ma J, Yang Y, Yuan Y (2004b) Simulation of the temperature and salinity along 36°N in the Yellow Sea with a wave–current coupled model. J Kor Soc Oceanogr 39(1):35–45

Qiao F, Yang Y, Lü X, Xia C, Chen X, Wang B, Yuan Y (2006) Coastal upwelling in the East China Sea in winter. J Geophys Res 111:C11S06. doi:10.1029/2005JC003264

Qiao F, Yang Y, Xia C, Yeli Y (2008) The role of surface waves in the ocean mixed layer. Acta Oceanolog Sin 27(3):30–37

Song Z, Qiao F, Yang Y, Yuan Y (2007) An improvement of the too cold tongue in the tropical Pacific with the development of an ocean–wave–atmosphere coupled numerical model. Prog Nat Sci 17(5):576–583

Stacey MW (1999) Simulations of the wind-forced near-surface circulation in Knight Inlet: a parameterization of the roughness length. J Phys Oceanogr 29:1363–1367

Terray EA, Donelan MA, Agrawal YC, Drennan WM, Kahma KK, III AJW, Hwang PA, Kitaigorodski SA (1996) Estimates of kinetic energy dissipation under breaking waves. J Phys Oceanogr 26:792–807

Xia C, Qiao F, Yang Y, Ma J, Yuan Y (2006) Three-dimensional structure of the summertime circulation in the Yellow Sea from a wave–tide–circulation coupled model. J Geophys Res 111:C11S03. doi:10.1029/2005JC003218

Yang Y, Qiao F, Zhao W, Teng Y, Yuan Y (2005) The development and application of the MASNUM wave numerical model in spherical coordinates. Acta Oceanolog Sin 27(2):1–7 (in Chinese)

Yu W, Qiao F, Yuan Y, Pan Z (1997) Numerical modeling of wind and waves for Typhoon Betty (8710). Acta Oceanolog Sin 16(4):459–473

Yuan Y, Hua F, Pan Z, Sun L (1991) LAGFD-WAM numerical wave model I. Basic physical model. Acta Oceanolog Sin 10(4):483–488

Yuan Y, Qiao F, Hua F, Wan Z (1999) The development of a coastal circulation numerical model: 1. Wave-induced mixing and wave–current interaction. J Hydrodyn Ser A 14:1–8 (in Chinese)